A&A 674, A54 (2023)
https://doi.org/10.1051/0004-6361/202245645

Astronomy & Astrophysics

Extended atomic data for oxygen abundance analyses*

W. Li[1], P. Jönsson[2], A. M. Amarsi[3], M. C. Li[4], and J. Grumer[3]

[1] National Astronomical Observatories, Chinese Academy of Sciences, Beijing 100012, PR China
e-mail: wxli@nao.cas.cn
[2] Department of Materials Science and Applied Mathematics, Malmö University, 205 06 Malmö, Sweden
[3] Theoretical Astrophysics, Department of Physics and Astronomy, Uppsala University, Box 516, 751 20 Uppsala, Sweden
[4] School of Electronic Information and Electrical Engineering, Huizhou University, Huizhou 516007, PR China

Received 8 December 2022 / Accepted 31 March 2023

ABSTRACT

As the most abundant element in the universe after hydrogen and helium, oxygen plays a key role in planetary, stellar, and galactic astrophysics. Its abundance is especially influential in terms of stellar structure and evolution, and as the dominant opacity contributor at the base of the Sun's convection zone, it is central to the discussion on the solar modelling problem. However, abundance analyses require complete and reliable sets of atomic data. We present extensive atomic data for O I by using the multiconfiguration Dirac–Hartree–Fock and relativistic configuration interaction methods. We provide the lifetimes and transition probabilities for radiative electric dipole transitions and we compare them with results from previous calculations and available measurements. The accuracy of the computed transition rates is evaluated by the differences between the transition rates in Babushkin and Coulomb gauges, as well as via a cancellation factor analysis. Out of the 989 computed transitions in this work, 205 are assigned to the accuracy classes AA-B, that is, with uncertainties smaller than 10%, following the criteria defined by the Atomic Spectra Database from the National Institute of Standards and Technology. We discuss the influence of the new $\log(gf)$ values on the solar oxygen abundance, ultimately advocating for $\log \epsilon_{\rm O} = 8.70 \pm 0.04$.

Key words. atomic data – Sun: abundances

1. Introduction

Oxygen is the most abundant metal in the universe. It is a key tracer of the evolution of galaxies (e.g. Romano 2022) as well as of the formation and characterisation of exoplanets (e.g. Kolecki & Wang 2022). In the interiors of stars, oxygen is a major source of opacity. For example, in the Sun, it is a dominant source near the base of the convection zone (e.g. Mondet et al. 2015). This makes the solar oxygen abundance critically important for resolving the solar modelling problem, which describes a significant discrepancy between theoretical predictions of the solar interior structure inferred from helioseismic inversions, as compared to standard solar models (e.g. Vinyoles et al. 2017; Christensen-Dalsgaard 2021).

The abundance of oxygen in stellar atmospheres can be determined from analyses of stellar spectra. In AFGK-type stars, one of the most commonly used oxygen abundance diagnostics, is the high-excitation O I 777 nm triplet (e.g. Nissen et al. 2014; Buder et al. 2021). Other permitted atomic features are sometimes used as well: most commonly the O I 615.8 nm (Korotin et al. 2014; Delgado Mena et al. 2021), and for the Sun, there is also the O I 844.7 nm and 926.9 nm multiplets (Asplund et al. 2004, 2021; Caffau et al. 2008). These are often complemented by low-excitation forbidden features, usually the [O I] 630.0 nm (Bertran de Lis et al. 2015; Franchini et al. 2021), and for the Sun, also the [O I] 557.7 nm and 636.3 nm lines (Allende Prieto et al. 2001; Meléndez & Asplund 2008), although at least in the solar spectrum these are significantly blended. Oxygen abundances can also be inferred from molecular diagnostics, in particular, the OH lines in the UV and infrared (Israelian et al. 1998; Boesgaard et al. 1999; Meléndez & Barbuy 2002). However, such lines are typically more sensitive to the effects of stellar convection (e.g. Asplund & García Pérez 2001; Amarsi et al. 2021).

The accuracy of abundance determinations is critically dependent on the reliability of radiative transition probability values. Moreover, if the assumption of local thermodynamic equilibrium (LTE) is to be relaxed, as is necessary for the O I 777 nm triplet and other high-excitation permitted atomic oxygen lines (e.g. Steffen et al. 2015; Amarsi et al. 2016), a broad set of reliable transition probabilities are needed to accurately determine the statistical equilibrium.

The vast majority of transition probabilities for atomic oxygen come from theoretical calculations. The transition probabilities and oscillator strengths of O I presented in the Atomic Spectra Database of the National Institute of Standards and Technology (NIST-ASD; see Kramida et al. 2022) were compiled by Wiese et al. (1996) based on the theoretical calculations from Hibbert et al. (1991), Butler & Zeippen (1991), and Biemont & Zeippen (1992). Hibbert et al. (1991) computed the oscillator strengths for a large number of allowed transitions connecting the $n \leq 4$ triplet and quintet states of neutral oxygen, using the CIV3 code. Butler & Zeippen (1991) performed the calculations of oscillator strengths for allowed transitions in O I, in the framework of the international Opacity Project. Using the computer program SUPERSTRUCTURE, Biemont & Zeippen (1992) calculated the oscillator strengths for 2p-3s and 3s-3p spin-allowed or spin-forbidden transitions of astrophysical interest.

There are also a number of other calculations available for O I. The complete lists of published papers can be retrieved

* Full Tables A.1 and A.2 are only available at the CDS via anonymous ftp to cdsarc.cds.unistra.fr (130.79.128.5) or via https://cdsarc.cds.unistra.fr/viz-bin/cat/J/A+A/674/A54

from the NIST Atomic Transition Probability Bibliographic database (Kramida 2023). Tachiev & Froese Fischer (2002) performed multi-configurational Hartree-Fock (MCHF) calculations including Breit-Pauli effects in subsequent configuration-interaction calculations and determined lifetimes and transitions rates for all fine-structure levels up to $2p^3 3d$ of the oxygen-like sequence (elements with atomic number Z = 8–20). Zheng & Wang (2002) calculated the atomic data, including the radiative lifetimes, transition probabilities, and oscillator strengths in O I, by employing the weakest bound electron potential model theory. Using the B-spline box-based R-matrix method in the Breit–Pauli formulation, Tayal (2009) calculated the oscillator strengths for allowed transitions among the n = 2–4 levels and from the n = 2 levels to higher excited levels up to n = 11 in neutral oxygen.

In this work, we present extended calculations of atomic data for the lowest 81 states in O I, using the multiconfiguration Dirac–Hartree–Fock (MCDHF) and relativistic configuration interaction (RCI) methods. These calculations are part of an overarching project concerning the astrophysically important CNO neutral elements and extensive results have already been reported earlier for C I (Li et al. 2021) and N I (Li et al. 2023). Electric dipole (E1) transition data (wavelengths, transition probabilities, line strengths, and weighted oscillator strengths) are computed, along with the corresponding lifetimes of these states. We then investigate how the differences in the calculated $\log(gf)$ may influence the solar oxygen abundance and thereby the solar modelling problem.

2. Theoretical method

2.1. Multiconfiguration Dirac–Hartree–Fock approach

Calculations were performed using the GRASP2018 package[1] (Froese Fischer et al. 2019; Jönsson et al. 2023), which is based on the MCDHF and RCI methods. Details of the MCDHF method can be found in Grant (2007), Froese Fischer et al. (2016, 2019), and Jönsson et al. (2022). Here, we only give a brief introduction. In the MCDHF method, wave functions Ψ for atomic states $\gamma^{(j)}\, PJM$, $j = 1, 2, \ldots, N$ with angular momentum quantum numbers JM and parity P are expanded over $N_{\rm CSFs}$ configuration state functions (CSFs):

$$\Psi(\gamma^{(j)}\, PJM) = \sum_{i}^{N_{\rm CSFs}} c_i^{(j)}\, \Phi(\gamma_i\, PJM). \tag{1}$$

The CSFs are jj-coupled many-electron functions built from products of one-electron Dirac orbitals. As for the notation, J and M are the angular quantum numbers, P is parity, and γ_i specifies the occupied subshells of the CSF with their complete angular coupling tree information, for example, orbital occupancy, coupling scheme, and other quantum numbers necessary to uniquely describe the CSFs.

The radial large and small components of the one-electron orbitals together with the expansion coefficients $\{c_i^{(j)}\}$ of the CSFs are obtained in a relativistic self-consistent field procedure, by solving the Dirac-Hartree-Fock radial equations and the configuration interaction eigenvalue problem resulting from applying the variational principle on the statistically weighted energy functional of the targeted states with terms added for preserving the orthonormality of the one-electron orbitals. The angular integrations needed for the construction of the energy functional are based on the second quantization method in the coupled tensorial form (Gaigalas et al. 1997, 2001) and account for relativistic kinematic effects. Once the radial components of the one-electron orbitals are determined, higher-order interactions, such as the transverse photon interaction and quantum electrodynamic effects (vacuum polarization and self-energy), are added to the Dirac-Coulomb Hamiltonian. Keeping the radial components fixed, the expansion coefficients $\{c_i^{(j)}\}$ of the CSFs for the targeted states are obtained by solving the configuration interaction eigenvalue problem.

The transition data, for example, transition probabilities, and weighted oscillator strengths between two states, $\gamma' P' J'$ and γPJ, are expressed in terms of reduced matrix elements of the transition operator $\mathbf{T}^{(1)}$:

$$\begin{aligned}&\langle\, \Psi(\gamma PJ)\, \|\mathbf{T}^{(1)}\|\, \Psi(\gamma' P' J')\, \rangle \\ &\quad = \sum_{j,k} c_j c'_k\, \langle\, \Phi(\gamma_j PJ)\, \|\mathbf{T}^{(1)}\|\, \Phi(\gamma'_k P' J')\, \rangle,\end{aligned} \tag{2}$$

where c_j and c'_k are, respectively, the expansion coefficients of the CSFs for the lower and upper states. The summation runs over all basis states included in the two CSF expansions Eq. (1).

2.2. dT and CF

In relativistic theory, there are two common representations of the E1 transition operator, namely, the Babushkin and Coulomb gauge, which are equivalent to the length and the velocity forms in the non-relativistic limit. Just as for the latter two, assuming the wavefunctions to be exact solutions to the Dirac equation leads to identical values for the Babushkin and Coulomb transition moments (Grant 1974).

For approximate solutions achievable in practise, the transition moments differ and the quantity dT, defined as

$$\mathrm{d}T = \frac{|A_{\rm B} - A_{\rm C}|}{\max(A_{\rm B}, A_{\rm C})}, \tag{3}$$

where $A_{\rm B}$ and $A_{\rm C}$ are transition rates in the Babushkin and Coulomb forms (Froese Fischer 2009; Ekman et al. 2014) can be used to evaluate the uncertainty of the computed rates in a statistical sense for a group of transitions.

The accuracy of the computed transition data can also be evaluated by studying the cancellation factor (CF), which is defined as (Cowan 1981)

$$\mathrm{CF} = \left[\frac{|\sum_j \sum_k c_j \langle\, \Phi(\gamma_j PJ)\, \|\mathbf{T}^{(1)}\|\, \Phi(\gamma'_k P' J')\, \rangle c'_k|}{\sum_k \sum_j |c_j \langle\, \Phi(\gamma_j PJ)\, \|\mathbf{T}^{(1)}\|\, \Phi(\gamma'_k P' J')\, \rangle c'_k|}\right]^2, \tag{4}$$

where the notations are the same as those in Eqs. (1) and (2). A small value of the CF, for example, less than 0.1 or 0.05 (Cowan 1981), indicates that the calculated transition parameter, such as the transition rate or line strength, is affected by a strong cancellation effect. This occurs due to the configuration interaction between basis states of opposite phase but almost equal amplitudes, resulting in a relatively small line strength. Transitions with small CFs are normally associated with large uncertainties; therefore, the CF can be used as a complement to the dT values for the uncertainty estimation. In this work, we extended the GRASP2018 package (Froese Fischer et al. 2019; Jönsson et al. 2023) to include the calculation of CFs.

[1] GRASP is fully open-source and is available on GitHub repository at https://github.com/compas/grasp maintained by the CompAS Collaboration.

Table 1. Summary of the computational schemes for O I.

Parity	MR in MCDHF	MR in RCI	AS	$N_{\rm CSFs}$
even	$2s^22p^3np$ ($n = 2-6$), $2s^22p^3nf$ ($n = 4, 5$)	$2s^22p^3np$ ($n = 2-8$), $2s^22p^3nf$ ($n = 4, 5$), $2s2p^4ns$ ($n = 3-7$), $2s2p^4nd$ ($n = 3-6$)	{12s, 12p, 11d, 11f, 9g, 7h}	12 641 532
odd	$2s^22p^3ns$ ($n = 3-6$), $2s^22p^3nd$ ($n = 3-5$)	$2s^22p^3ns$ ($n = 3-7$), $2s^22p^3nd$ ($n = 3-5$)	{12s, 12p, 11d, 11f, 9g, 7h}	7 683 274

Notes. MR and AS, respectively, denote the multireference and the active sets of orbitals used in the calculations. $N_{\rm CSFs}$ are the numbers of generated CSFs in the final RCI calculations.

2.3. Computational schemes

Calculations were performed in the extended optimal level (EOL) scheme (Dyall et al. 1989) for the weighted average of the even states (up to $2s^22p^35f$) and odd states (up to $2s^22p^35d$). The CSF expansions were obtained using the multireference single-double (MR-SD) method, allowing for single and double (SD) substitutions from MR configurations to orbitals in an active set (AS; Olsen et al. 1988; Sturesson et al. 2007; Froese Fischer et al. 2016).). In addition to the target configurations representing the physical states, a number of configurations giving considerable contributions to the total wave functions are also included in the MR. Furthermore, SD substitutions from such an extended MR has the effect of including higher order configuration-interaction contributions in the wave functions (relative to the target configurations). The two MR sets for the even and odd parities are presented in Table 1, which also displays the AS and the number of CSFs in the final even and odd state expansions distributed over the different J symmetries.

Similarly to the computational schemes used in C I-IV (Li et al. 2021) and N I (Li et al. 2023) and following the CSF generation strategies suggested by Papoulia et al. (2019), the MCDHF calculations were based on CSF expansions for which we imposed restrictions on the substitutions from the inner subshells to obtain a better representation of the outer parts of the wave functions of the higher Rydberg states. As a consequence, we were able to improve the accuracy of the transition data. In the initial calculations, we investigated the contribution of the core-valence (CV) correlations to the results by allowing at most one substitution from $1s^2$ and found that the CV contributions are negligible. Therefore, the $1s^2$ core remained frozen in both the MCDHF and RCI calculations. The CSF expansions used in the subsequent MCDHF calculations were obtained by allowing SD substitutions from the 2p orbital of the target configurations to the active set of orbitals. During this stage, the 1s and 2s orbitals were kept closed. The final wave functions of the targeted states were determined in an RCI calculation, which included CSF expansions that were formed by allowing SD substitution from all subshells with $n = 2$ of the MR configurations.

3. Results and discussions

3.1. Energy levels and lifetimes

The energies for the 81 lowest states of O I (45 even states and 36 odd states) are given in Table A.1. In the calculations, the labelling of the eigenstates is determined by the CSF with the largest coefficient in the expansion of Eq. (1). For comparison, the observed energies from the NIST-ASD (Kramida et al. 2022), together with the differences $\Delta E = E_{\rm NIST} - E_{\rm MCDHF}$ are also displayed in the table. In most cases, the relative differences between theoretical and experimental results are less than 0.2%, with the exception of the levels belonging to the ground configuration $2s^22p^4$, for which the average relative difference is about 1.16%. Figure 1 shows the energy differences between NIST-ASD values and the present computed data, ΔE, plotted against the excitation energies, $E_{\rm RCI}$. From the linear fitting we can see that the computational excitation energies have a systematic error of 0.25%. We observed that for most of the levels, the computed results are smaller than the NIST-ASD values by about 170–190 $\rm cm^{-1}$ except for a few states belonging to $2s^22p^4$ and $2s^22p^33s$. By excluding these levels, that is, $2s^22p^4\ {}^1D_2$, $^1S_0$, $2s^22p^33s\ {}^5S_2$, $^3S_1$, $^3D_{1,2,3}$, and $^1D_2$, the systematic error decreased to 0.19%. In the last two columns of Table A.1, lifetimes obtained from the computed E1 transition rates in both Babushkin and Coulomb gauges are also presented. The relative differences between the Babushkin and Coulomb gauges are well below 5%, except for a few states for which decay to the lower states is dominated by intercombination transitions.

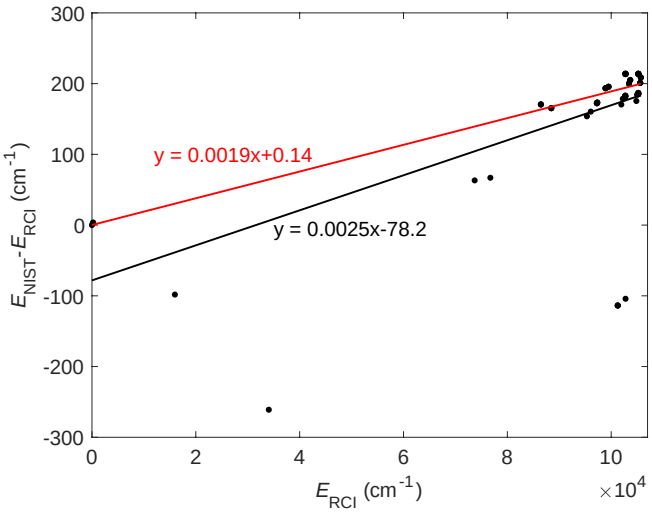

Fig. 1. Energy differences along with present computed excitation energies. The black solid line is the linear fit to the scatter data shown in the figure. The red solid line is the linear fit by excluding the $2s^22p^4\ {}^1D_2$, $^1S_0$, $2s^22p^33s\ {}^5S_2$, $^3S_1$, $^3D_{1,2,3}$, and $^1D_2$ states.

In Table 2, the lifetimes from the present MCDHF/RCI calculations are compared with available results from other theoretical calculations and experimental measurements. The calculated lifetimes in the Babuskin and Coulomb forms are consistent to 6.0% for all the selected transitions. Among others, atomic properties of the metastable state $2p^33s\ {}^5S^o_2$ are interesting due to its potential in astrophysical diagnosis. The lifetime of the $2p^33s\ {}^5S^o_2$ state has been studied systematically using

Table 2. Comparison of lifetimes in both Babushkin (B) and Coulomb (C) gauges, B/C, with other theoretical (Other theo.) and experimental (Exp.) results.

		Lifetimes		
State	Unit	Present	Other theo.	Exp.
$2p^3 3s\ ^5S^o$	μs	209/213	528 [a], 202/235 [d], 200 [e]	170±25 [f], 185±10 [g], 180±5 [h], 185±30 [i]
$2p^3 3s\ ^3S$ [o]	ns	1.70/1.69	1.76 [a],1.61 [b], 1.73 [c], 1.63 [e]	2.4±0.3 [j], 1.7±0.3 [k], 1.7±0.2 [l], 1.82±0.05 [r], 1.79±0.17 [p], 1.70±0.15 [m], 1.70±0.14 [n], 1.8±0.27 [o]
$2p^3 3s\ ^3D$ [o]	ns	4.21/4.15	4.19 [b], 4.46 [c]	3.94±0.22 [p], 5.0±0.4 [q], 4.5±0.675 [o]
$2p^3 3s\ ^1D$ [o]	ns	1.86/1.85		1.77±0.14 [p], 2.01±0.12 [q]
$2p^3 4s\ ^3S$ [o]	ns	5.74/5.67	5.33 [a], 5.24 [b], 5.04 [c]	4.0±0.6 [o]
$2p^3 5s\ ^3S$ [o]	ns	13.55/13.35		17±3 [s], 6.0±0.9 [o]
$2p^3 6s\ ^3S$ [o]	ns	26.82/25.22		24±3 [s]
$2p^3 3p\ ^3P$	ns	32.12/32.73	32.70 [a], 29.68 [b]	36±4 [s], 39.1±1.4 [t], 40±3 [u]
$2p^3 4p\ ^3P$	ns	182.3/181.8	175.4 [b]	153±10 [u], 161±19 [v]
$2p^3 4p\ ^5P$	ns	200.2/212.0	189.7 [b]	193±10 [u], 194±19 [v]
$2p^3 4d\ ^5D$ [o]	ns	72.15/73.21	72.20 [b], 96.64 [c]	96±4 [u], 95±9 [v]
$2p^3 4d\ ^3D$ [o]	ns	15.31/15.41	16.85 [b], 12.91 [c]	23±3 [s], 20±3 [o], 80±10 [u]
$2p^3 5d\ ^3D$ [o]	ns	31.13/32.12		36±4 [s], 30±4.5 [o]

Notes. The experimental uncertainties for results from Brooks et al. (1977) are given with the upper limit of the uncertainties, i.e. 15%.

References. [a]Tachiev & Froese Fischer (2002); [b]Hibbert et al. (1991); [c]Tayal (2009); [d]Zhang et al. (2020); [e]Biemont & Zeippen (1992); [f]Wells & Zipf (1974); [g]Johnson (1972); [h]Nowak et al. (1978); [i]Mason (1990); [j]Savage & Lawrence (1966); [k]Gaillard & Hesser (1968); [l]Druetta & Poulizac (1970); [m]Martinson et al. (1971); [n]Lin et al. (1972); [o]Brooks et al. (1977); [p]Smith et al. (1971); [q]Pinnington et al. (1974); [r]Lawrence (1970); [s]Kröll et al. (1985); [t]Bischel et al. (1981, 1982); [u]Bromander et al. (1978); [v]Day et al. (1981).

the MCDHF method by Zhang et al. (2020) and the final values of 202±30 μs in the Babuskin gauge and 235±35 μs in the Coulomb gauge were recommended. Our calculated results of 209/213 μs (in B/C forms) are in good agreement with their values. The much larger lifetime from the MCHF calculation by Tachiev & Froese Fischer (2002) is likely caused by neglected electron correlation and relativistic effects. However, the theoretical lifetimes from the various calculations are still larger than the experimental values reported in Wells & Zipf (1974), Johnson (1972), Nowak et al. (1978), and Mason (1990), obtained using the time-of-flight technique. It is also interesting to note that the theoretical lifetimes from Tayal (2009), based on the B-spline box-based R-matrix method, for 3s $^3D^o$, 4s $^3S^o$, 4d $^5D^o$, and 4d $^3D^o$ states, differ significantly from those obtained with the other three theoretical approaches, which are Tachiev & Froese Fischer (2002) using the MCHF method implemented in the ATSP code (Froese Fischer 2000; Froese Fischer et al. 2007), and the configuration interaction (CI) calculations of Hibbert et al. (1991) and Biemont & Zeippen (1992) the CIV3 (Hibbert 1975) and SUPERSTRUCTURE codes (Eissner 1991), respectively.

There are a number of lifetime measurements in O I presented in, for example, Brooks et al. (1977) using the electron-beam phase-shift method, Kröll et al. (1985) from the time-resolved laser spectroscopy, as well as Smith et al. (1971) and Pinnington et al. (1974), using the beam foil technique. The measurements of Brooks et al. (1977) agree within the experimental errors with our calculated lifetimes for the 3s $^3S^o$,$^3D^o$, and 5d $^3D^o$ states, while showing large discrepancies for 4s, 5s $^3S^o$, and 4d $^3D^o$ states. Our lifetimes of 3s $^3S^o$,$^3D^o$, and $^1D^o$ states agree well with the experimental results published by Smith et al. (1971) using the beam-foil method; whereas Pinnington et al. (1974), who utilized the same experimental technique, measured somewhat larger values. Time-resolved spectroscopy and high frequency deflection technique were used, respectively, by Kröll et al. (1985) and Bromander et al. (1978) for measuring the lifetimes of *ns*, *np,* and *nd* states in O I. The results from Kröll et al. (1985) are consistent with our theoretical lifetimes within the experimental errors, while the results from Bromander et al. (1978) are either too large or too small, when compared with the theoretical predicted values. For 3s $^3S^o$ state, our results agree well with all the experimental data if we exclude the lifetime value from Savage & Lawrence (1966), which is evidently too large.

3.2. Transition rates and oscillator strengths

Transition data in the form of wavelengths, line strengths (S), weighted oscillator strengths ($\log(gf)$), transition probabilities (A), gauge agreements, dT, and cancellation factors, CF, as well as the estimated accuracy classes of all computed E1 transitions are given in Table A.2. It is important to note that the reported wavelengths have been adjusted to match the level energy values in the NIST-ASD. The data for $\log(gf)$ and A are reported in both Babuskin and Coulomb gauge and are adjusted using experimental wavelengths.

3.2.1. Comparisons with previous theoretical results

The calculated transition results were compared with findings from other theoretical works. In the left panel of Fig. 2, A values in both Babushkin and Coulomb gauges from the present work are compared with available data from the NIST-ASD (Kramida et al. 2022), which are compiled based on the results from Hibbert et al. (1991), Biemont & Zeippen (1992), and Butler & Zeippen (1991). The first two calculations were carried out using the CIV3 and SUPERSTRUCTURE code, respectively. The

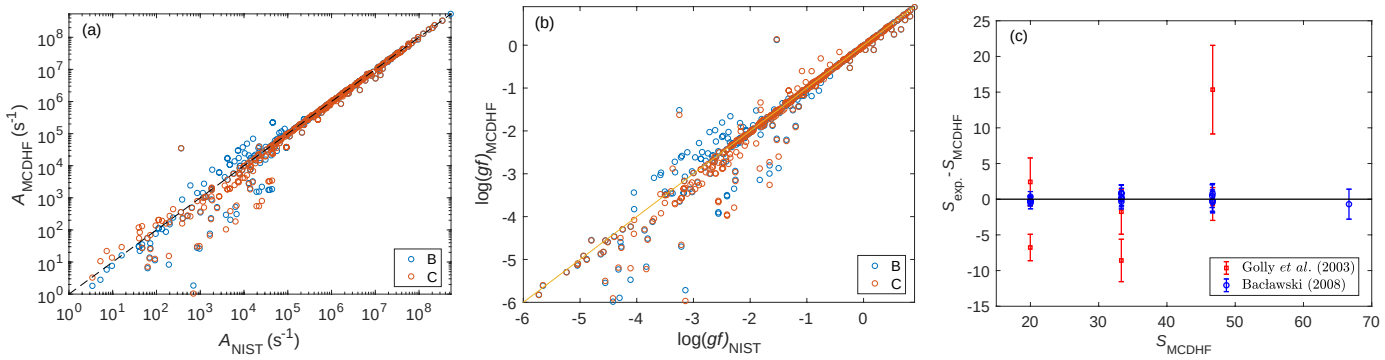

Fig. 2. Comparison of transition data of the current study with the values from other work. Panel a: comparison of theoretical transition probabilities, A, in both Babushkin (B) and Coulomb (C) gauge with the results available in the NIST-ASD (Kramida et al. 2022). Panel b: comparison of the log(gf) values in Babushkin form with the results from CIV3 (Hibbert et al. 1991), MCHF (Tachiev & Froese Fischer 2002) and B-spline R-matrix (Tayal 2009) calculations. Panel c: comparison of the theoretical line strengths, $S_{\rm MCDHF}$, with the corresponding experimental results published by Golly et al. (2003, in red square) and Bacławski (2008, in blue circle). Note: Relative line strengths were provided by Bacławski (2008), which means that the line strengths are normalised within each multiplet to the sum of 100; the corresponding results from present calculations and Golly et al. (2003) were done with the same procedure. The line strengths in Babushkin gauge were used for the comparison.

latter work was done within the framework of the international Opacity Project.

As shown in the figure, the agreement between the A values computed in the present work and the respective results from the NIST-ASD is rather good for most transitions, especially for transitions with $A_{\rm B} \geq 10^5$ s^{-1}. In taking the results in the Babuskin gauge as example, 70% of the 380 selected transitions are in agreement with the NIST-ASD data, with the differences being less than 20%. 204 out of the 236 transitions having $A_{\rm B}$ $\geq 10^5$ are in agreement with the NIST-ASD data, with the relative differences being less than 10%. It is interesting to note that for transitions with $10^3 \leq A \leq 10^5$ s^{-1}, the transition data in the Coulomb gauge are more consistent with the results in the NIST-ASD than those in the Babushkin gauge. On closer inspection of these transitions, we found that most of them are transitions involving high Rydberg states. For example, 74% of them are those from $n = 5, 6$ states to lower levels. For this class of transitions, we recommend the radiative data calculated in the Coulomb gauge – and not the more conventional Babuskin gauge. Following Papoulia et al. (2019), the reason for this is that correlation orbitals resulting from MCDHF calculations based on CSF expansions obtained by including substitutions from deeper subshells are contracted, in comparison with the outer Rydberg orbitals. As a consequence, the outer parts of the wave functions for the relatively extended Rydberg states are not accurately described. Thus, it can be argued that the Coulomb gauge, which is weighted on the inner parts of the wavefunction, should yield more reliable transition data than the Babushkin gauge for transitions involving high-lying Rydberg states. However, for transitions involving low-lying states, our calculated transition rates in two gauges are very consistent with each other, except for some weak transitions with $A < 10^2$ s^{-1}; for these transitions with large differences between two gauges, the Babushkin form is generally preferred, since it is more sensitive to the outer part of the wave functions that governs the atomic transitions (Grant 1974; Hibbert 1974).

Furthermore, in the middle panel of Fig. 2, the computed log(gf) values in the Babushkin gauge are compared with the results from various calculations of Tayal (2009), Tachiev & Froese Fischer (2002), and Hibbert et al. (1991), which were carried out by B-spline R-matrix, CI, and MCHF methods, respectively. From the figure, we note an excellent agreement between the present results and the other three theoretical values for transitions with log(gf) > −1.5. However, for weaker transitions with log(gf) < −1.5, the agreement between different methods is worse with a much wider scatter. Overall, the log(gf) values from the present work are in better agreement with those from Tachiev & Froese Fischer (2002) and Hibbert et al. (1991) than those from Tayal (2009).

3.2.2. Comparisons with available experimental results

In Table 3, the computed gf values are compared with some available results from experimental measurements. Goldbach & Nollez (1994) measured the log(gf) values of 12 lines of O I belonging to five multiplets in the 95–120 nm spectral range with a wall-stabilized arc. The uncertainty achieved in the measured absolute gf-values is between ±10 and ±20%. Our computed gf results in both gauges are in excellent agreement with the measured values by Goldbach & Nollez (1994), except for the 115.215 nm and 99.080 nm lines, for which we predicted slightly larger values (by 2%). For the 115.215 nm line, other determinations of gf values have also been achieved by utilizing various techniques, for instance, the beam-foil technique (Smith et al. 1971; Martinson et al. 1971; Lin et al. 1972; Pinnington et al. 1974), phase-shift technique (Gaillard & Hesser 1968), or pulsed electron beam (Lawrence 1970). From Table 3, we note that different methods obtained very consistent results, and our computed values are in good agreement with them. A number of measurements of gf values have also been done for the 130.6 nm line. Again, the results from different measurements agree perfectly with each other, as well as with our computed results in both Babushkin and Coulomb gauges. In addition, Bridges & Wiese (1998) measured the transition probabilities of the $2p^3 3s\ ^3S^o – 4p\ ^3P$ and $3s\ ^5S^o – 2p^3 4p\ ^5P$ arrays and obtained the values of 7.62 ×10^5 s^{-1} and 3.64 ×10^5 s^{-1}, respectively. Our computed results are in agreement with the experimental value for the $2p^3 3s\ ^3S^o – 2p^3 4p\ ^3P$ array within the experimental error, while predicting a slightly larger transition probability for the $2p^3 3s\ ^5S^o – 2p^3 4p\ ^5P$ array, that is, by about 5% after considering the experimental uncertainty.

There are also measurements of line strengths for spectral lines in the visible and infrared (Golly et al. 2003; Bacławski 2008). In Fig. 2c, the computed S values in Babushkin gauge are compared with experimental results from Golly et al. (2003)

Table 3. Comparison of gf values in both Babushkin (B) and Coulomb (C) gauges, B/C, with available experimental (Exp.) results.

			gf		
Upper	Lower	$\lambda_{\rm vac.}$ (nm)	Present	Exp. [a]	Other exp.
$2p^3 3s\ ^3S^o_1$	$2p^4\ ^3P_0$	130.603	0.0499/0.0501		0.05±0.01 [b], 0.05±0.005 [c], 0.047±0.0014 [d], 0.047±0.0047 [e], 0.048±0.0048 [f], 0.050±0.0050 [g], 0.05±0.0115 [h], 0.052±0.0052 [i], 0.045±0.009 [j], 0.053±0.00318 [k]
$2p^3 3s\ ^1D^o_2$	$2p^4\ ^1D_2$	115.215	0.535/0.538	0.49±0.039	0.526±0.083 [b], 0.526±0.055 [d], 0.56±0.04 [e], 0.50±0.05 [f], 0.51±0.026 [g], 0.50±0.03 [l]
$2p^3 4s\ ^3S^o_1$	$2p^4\ ^3P_0$	104.169	0.00827/0.00841	0.0089±0.0015	
$2p^3 4s\ ^3S^o_1$	$2p^4\ ^3P_1$	104.094	0.0249/0.0252	0.029±0.0049	
$2p^3 4s\ ^3S^o_1$	$2p^4\ ^3P_2$	103.923	0.0417/0.0423	0.048±0.0072	
$2p^3 3d\ ^3D^o_{1,2}$	$2p^4\ ^3P_1$	102.743	0.0627/0.0624	0.069±0.010	
$2p^3 3d\ ^3D^o_1$	$2p^4\ ^3P_0$	102.816	0.0209/0.0208	0.024±0.0031	
$2p^3 3s\ ^3D^o_1$	$2p^4\ ^3P_0$	99.080	0.0570/0.0577	0.052±0.0047	
$2p^3 3s\ ^3D^o_1$	$2p^4\ ^3P_1$	99.013	0.0442/0.0448	0.042±0.0042	
$2p^3 3s\ ^3D^o_2$	$2p^4\ ^3P_1$	99.020	0.128/0.130	0.11±0.0121	
$2p^3 3s\ ^3D^o_2$	$2p^4\ ^3P_2$	98.865	0.0457/0.0463	0.051±0.0071	
$2p^3 3s\ ^3D^o_3$	$2p^4\ ^3P_2$	98.877	0.243/0.246	0.22±0.044	

Notes. The results from present calculations are adjusted to experimental wavelengths.

References. [a]Goldbach & Nollez (1994); [b]Gaillard & Hesser (1968); [c]Druetta & Poulizac (1970); [d]Lawrence (1970); [e]Smith et al. (1971); [f]Martinson et al. (1971); [g]Lin et al. (1972); [h]Ott (1971); [i]Kikuchi (1971); [j]Clyne & Piper (1976); [k]Jenkins (1985); [l]Pinnington et al. (1974).

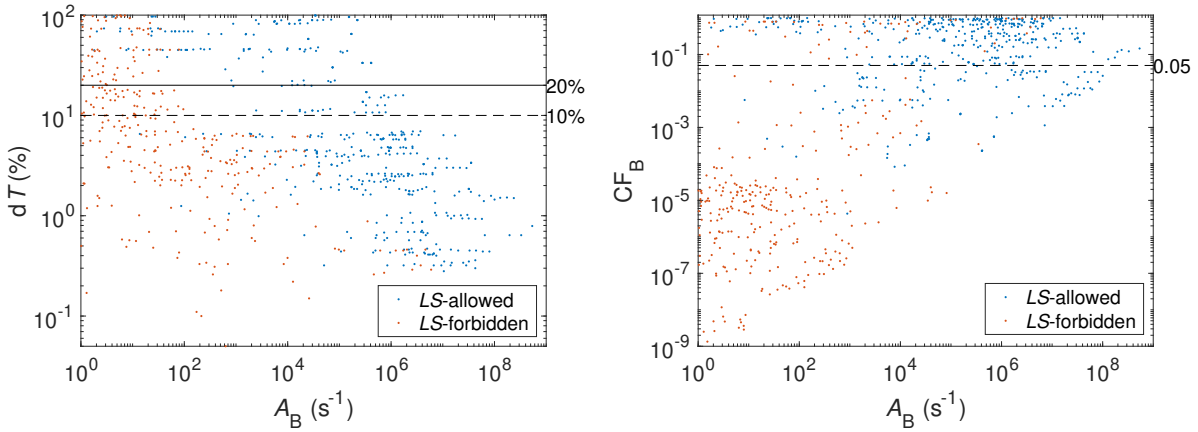

Fig. 3. Scatterplot of dT and CF values versus transition rates A of E1 transitions, for O I. Left panel: scatterplot of dT values versus transition rates in Babushkin form, $A_{\rm B}$, of E1 transitions with $A_{\rm B} > 10^0$ s^{-1}. Right panel: same as the left panel but for cancellation factor, CF. *LS*-allowed and *LS*-forbidden transitions are marked in blue and red, respectively.

and Bacławski (2008) by plotting line strength differences versus the computed line strengths. We note that Bacławski (2008) provided the relative line strengths within multiplets (normalised to 100); therefore, all the values used for comparison in Fig. 2c are converted to the relative values. We can see that all of our computed lines strengths are in agreement with the results from Bacławski (2008) within the reported experimental uncertainties. However, in comparison with the results by Golly et al. (2003), large discrepancies are observed for the $2p^3 3p\ ^5P$–$2p^3 3d\ ^5D^o$ transition array, for which our computed results are in perfect agreement with those from Bacławski (2008).

3.2.3. Uncertainty estimation using dT and CF

There are a number of methods being used for estimation of uncertainties of calculated transition rates (Kramida 2014; Froese Fischer 2009; Ekman et al. 2014; El-Sayed 2021; Gaigalas et al. 2020). However, the estimation of uncertainties of calculated transition rates is not trivial and different methods may only applicable to specific systems and ionisation stages. In this work, as discussed in Sect. 2.2 and as shown in Eqs. (3) and (4), we attempted to evaluate the uncertainties using the dT and CF values.

Figure 3 shows the scatterplots of dT (left panel) and CF (right panel, in Babushkin gauge) versus A (in Babushkin gauge). We note that the weak transitions with transition rates $A < 10^0$ s^{-1} are neglected in the figure due to the fact that these weak transitions tend to be of lesser astrophysical importance, either for opacity calculations or for spectroscopic abundance analyses. In the figure, we depict the *LS*-allowed and *LS*-forbidden transitions in different colours. Overall, as can be seen from Fig. 3, stronger transitions with larger A rates or *LS*-allowed

Table 4. Distribution of dT (in %) and CF of the computed transition rates in O I depending on the magnitude of the transition rates.

Group	A (s^{-1})	No.	$\langle dT \rangle$ (%)	$dT < 20\%$ (& CF > 0.05) (%)	$dT < 10\%$ (& CF > 0.05) (%)	$dT < 5\%$ (& CF > 0.05) (%)
g1	10^0–10^2	226	28.32	58.8 (0.4)	38.1 (0.4)	23.5 (0.0)
g2	10^2–10^4	147	17.03	74.8 (24.5)	72.1 (23.1)	57.1 (12.2)
g3	10^4–10^6	221	17.99	75.6 (65.2)	63.3 (54.3)	52.5 (45.7)
g4	10^6–	166	2.29	100.0 (95.8)	98.8 (94.6)	86.7 (82.5)

Notes. The analysis is done based on the data adjusted to experimental wavelengths.

Table 5. Connection of the limits of dT or d$\tilde{T}$ and CF for the accuracy classes (Acc.).

Acc.	Unc. (%)	dT or d$\tilde{T}$ (%)	CF	N	$N_{acc.}$ g1	g2	g3	g4
A	≤3	≤3	≥0.1	80	0	0	0	80
B	≤10	>3 & ≤10	≥0.1	125	0	0	41	84
		≤3	<0.1					
C	≤25	>10 & ≤25	≥0.1	317	70	111	134	2
		>3 & ≤10	<0.1					
D	≤50	>25 & ≤50 or >10 & ≤25	≥0.1 <0.1	269	110	20	19	0
E	>50	>50 >25 & ≤50	<0.1	198	46	16	27	0

Notes. N is the total number of computed transitions belonging to a specific accuracy class obtained from the d$\tilde{T}$ indicator. $N_{acc.}$ is the number of transitions belonging to a specific accuracy class in each transition group defined in Table 4. Note: the CF in the Babushkin gauge is used in this statiscal analysis. The A, B, C, D, and E classes include, respectively, the {A, A+, and AA}, {B+ and B}, {C+ and C}, {D+ and D}, and E classes as defined by the NIST-ASD. The corresponding uncertainty (Unc.) limits are shown in the second column.

transitions are always associated with smaller dT and larger CF values, which indicate that these transitions have small uncertainties. However, the weak transitions, which are mostly the *LS*-forbidden intercombination transitions, are associated with smaller CFs and are strongly affected by cancellations. The mean dT (CF) for all E1 transitions shown in Fig. 3 is 17.4% (0.27).

To better display the dT and CF parameters of the computed transitions rates and their distribution in relation to the magnitude of the transition rates A, we organised the transitions into four groups (g1–g4) based on the magnitude of A values, as shown in Table 4. The first three groups contain the weak transitions with A up to 10^6 s^{-1}, while the last group contains the strong transitions with $A \geq 10^6$ s^{-1}. The average value of the $\langle dT \rangle$ is given for each group. The $\langle dT \rangle$ is only 2.29% for the fourth group transition, which indicates a very high accuracy achieved for the strong transitions with $A \geq 10^6$ s^{-1}. In addition, the statistical analysis of the proportions of transitions with CF > 0.05 and/or different dT values, that is, $dT < 20\%$, $dT < 10\%$, and $dT < 5\%$, for each group of transitions was also performed, with results shown in the last three columns of Table 4.

Based on the dT and CF values, we estimated the accuracy class for each transition using four procedures. The first one adopts the dT value defined in Eq. (3) as the uncertainty for each transition rate. For the second procedure, the definition of dT and CF for each of the accuracy classes are presented in Table 5. Furthermore, in the third approach, we organised the transitions into six groups based on the magnitude of A values, that is, $A < 10^{-2}$ s^{-1}, $10^{-2} \leq A < 10^1$ s^{-1}, $10^1 \leq A < 10^3$ s^{-1}, $10^3 \leq A < 5{\times}10^5$ s^{-1}, $5{\times}10^5 \leq A < 3.5{\times}10^6$ s^{-1}, and $A \geq 3.5{\times}10^6$, and calculated the averaged dT_{av} for each group. Then we defined $d\tilde{T} = \max(dT, dT_{av})$ to replace the dT as the uncertainty of each particular transition rate. Finally, the fourth procedure employs the definition of d$\tilde{T}$ and CF given in Table 5 as the uncertainty indicator. The statistical analysis of the number of transitions belonging to a specific accuracy class was performed. The percentage fractions obtained from the four methods are shown in Fig. 4.

From the comparison between the dT and dT&CF methods, we can see that the accuracy of some of the A class transitions is degraded according to the value of CF, for example, the percentage fraction is decreased from 28.7% to 14.7% for the A class transitions. Compared to the other two indicators, d$\tilde{T}$ and d$\tilde{T}$&CF predicted rather low percentage fractions of transitions in high-accuracy category having uncertainties less than 10%, which are 8.0% and 5.2%, respectively. From Fig. 4, using the dT values only for accuracy estimations might underestimate the uncertainties. As concluded in Ekman et al. (2014), dT is a reliable indicator of uncertainties of transition rates, especially for *LS*-allowed transitions; while for *LS*-forbidden transitions, dT can be used as uncertainties indicators if averaging over a large sample. Therefore, the d$\tilde{T}$ and d$\tilde{T}$&CF indicators may yield a 'safer' uncertainty estimation of the calculated transition rates, although they may overestimate the uncertainties, especially for the strong *LS*-allowed transitions.

The accuracy classes predicted from the d$\tilde{T}$ procedure are given in Table A.2. A statistical analysis was performed on the distributions of accuracy classes, with the results shown in Table 5. Overall, 80 (205) out of 989 computed transitions in this work have a uncertainty of <3% (<10%) and assigned to accuracy class A (B). Among the 80 transitions belonging to the A accuracy class, all are rather strong, with $A \geq 10^6$ s^{-1} (g4).

Table 6. Allowed O I lines used as oxygen abundance diagnostics.

Upper	Lower	λ_{air}(nm)	log gf					
			Present		NIST [a]	QDT [b]	Multi-method [c]	Multi-method [d]
			B	C				
$2p^3 4d\ ^5D^o_2$	$2p^3 3p\ ^5P_3$	615.815	–1.849	–1.851	–1.841			
$2p^3 4d\ ^5D^o_3$	$2p^3 3p\ ^5P_3$	615.817	–1.004	–1.006	–0.995			
$2p^3 4d\ ^5D^o_4$	$2p^3 3p\ ^5P_3$	615.819	–0.418	–0.420	–0.409			
$2p^3 3p\ ^5P_3$	$2p^3 3s\ ^5S^o_2$	777.194	0.350	0.335	0.369	0.317	0.350	0.350±0.021
$2p^3 3p\ ^5P_2$	$2p^3 3s\ ^5S^o_2$	777.417	0.204	0.189	0.223	0.170	0.204	0.196±0.022
$2p^3 3p\ ^5P_1$	$2p^3 3s\ ^5S^o_2$	777.539	-0.018	–0.033	0.002	–0.051	–0.019	–0.0296±0.021
$2p^3 3p\ ^3P_0$	$2p^3 3s\ ^3S^o_1$	844.625	–0.466	–0.474	–0.463	–0.493		
$2p^3 3p\ ^3P_2$	$2p^3 3s\ ^3S^o_1$	844.636	0.233	0.225	0.236	0.206		
$2p^3 3p\ ^3P_1$	$2p^3 3s\ ^3S^o_1$	844.676	0.011	0.003	0.014	–0.015		
$2p^3 3d\ ^5D^o_2$	$2p^3 3p\ ^5P_3$	926.583	–0.739	–0.737	–0.718	-0.750		
$2p^3 3d\ ^5D^o_3$	$2p^3 3p\ ^5P_3$	926.594	0.106	0.108	0.125	0.096		
$2p^3 3d\ ^5D^o_4$	$2p^3 3p\ ^5P_3$	926.601	0.693	0.694	0.712	0.681		
$2p^3 4s\ ^5S^o_2$	$2p^3 3p\ ^5P_3$	1130.238	0.056	0.040	0.078	0.033		
$2p^3 4s\ ^3S^o_1$	$2p^3 3p\ ^3P_1$	1316.389	–0.258	–0.263	–0.254	–0.280		
$2p^3 4s\ ^3S^o_1$	$2p^3 3p\ ^3P_2$	1316.485	–0.036	–0.041	–0.032	–0.058		
$2p^3 4s\ ^3S^o_1$	$2p^3 3p\ ^3P_0$	1316.511	–0.735	–0.740	–0.731	–0.757		

Notes. Shown are the upper and lower configurations, experimental wavelength (nm in air), and oscillator strengths obtained from various calculations. The log (gf) values in the penultimate column for the 777-triplet lines given by Magg et al. (2022) are based on the results calculated with both the GRASP and AUTOSTRUCTURE code. The values in the last column reported by Bautista et al. (2022) are obtained by averaging over results from multiple methods (MCDHF, R-matrix, pseudo-relativistic Hartree-Fock method+core-polarization effects, and CI).The log (gf) results from the present calculation are adjusted using experimental wavelengths.

References. [a]Kramida et al. (2022); [b]Civiš et al. (2018); [c]Magg et al. (2022); [d]Bautista et al. (2022).

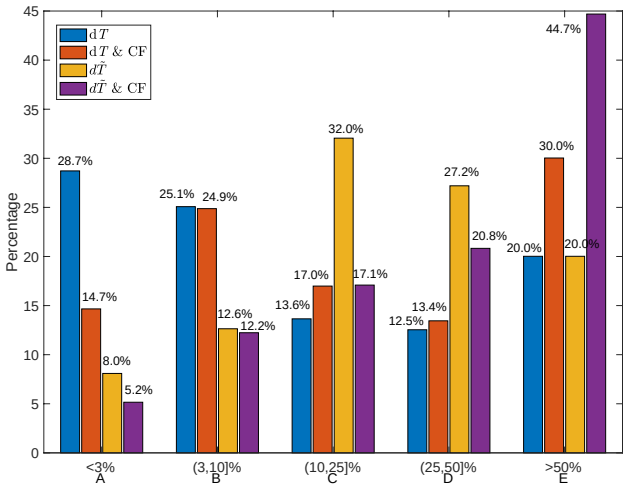

Fig. 4. Percentage fractions of all transitions in O I in different uncertainty categories: A (uncertainty ≤ 3%), B (3% < Uncertainty ≤ 10%), C (10% < uncertainty ≤ 25%), D (25% < Uncertainty ≤ 50%), and E (uncertainty > 50%), for the uncertainty estimate based on dT values only (blue), dT&CF values (red), d$\tilde{T}$ (orange), and d$\tilde{T}$&CF values (purple).

All the transitions in g4 are associated with uncertainties less than 25%; while for group g1, most transitions are assigned to accuracy classes C, D, or E.

4. Solar oxygen abundance

The solar oxygen abundance is still a subject of heated debate. It has undergone a major downward revision in recent decades, going from $\log \epsilon_O \equiv \log N_O/N_H + 12 = 8.93$ in Anders & Grevesse (1989) to 8.66 in Asplund et al. (2005). Recent estimates can be separated into 'low' values of $\log \epsilon_O = 8.67$–8.71 (Amarsi et al. 2018, 2021; Asplund et al. 2021) and 'intermediate' values of 8.73–8.77 (Caffau et al. 2015; Steffen et al. 2015; Bergemann et al. 2021; Magg et al. 2022), with 'high' values in the range 8.80–8.90 also having been suggested (Socas-Navarro 2015; Cubas Armas et al. 2020).

One of the differences between the recent studies of Amarsi et al. (2018) and Asplund et al. (2021), regarding low oxygen abundances, and Bergemann et al. (2021) and Magg et al. (2022), intermediate oxygen abundances, are the transition probabilities for their O I lines. In the former case, the transition probabilities for the O I 615.8 nm, 777 nm, 844.7 nm, and 926.9 nm features were taken from the NIST-ASD and are based on the atomic data of Hibbert et al. (1991). On the other hand, the latter two studies, based solely on the O I 777 nm triplet, draw on calculations from Civiš et al. (2018) that were computed using the quantum defect theory (QDT), as well as those from Bautista et al. (2022), based on an average over results from multiple methods.

Table 6 presents the permitted lines that have been adopted by different solar oxygen abundance analyses (Asplund et al. 2004, 2021; Caffau et al. 2008). The log(gf) values for these lines from various calculations are given in the table. It is interesting to note that in all cases, the log(gf) values from the NIST-ASD (based on Hibbert et al. 1991) are systematically larger than the other theoretical results. Compared to our results in the Babushkin gauge, these are too small by between 0.01 to 0.02 dex. In addition, the QDT values of Civiš et al. (2018) are systematically smaller than the values from the other calculations. The differences with regard to our results are between

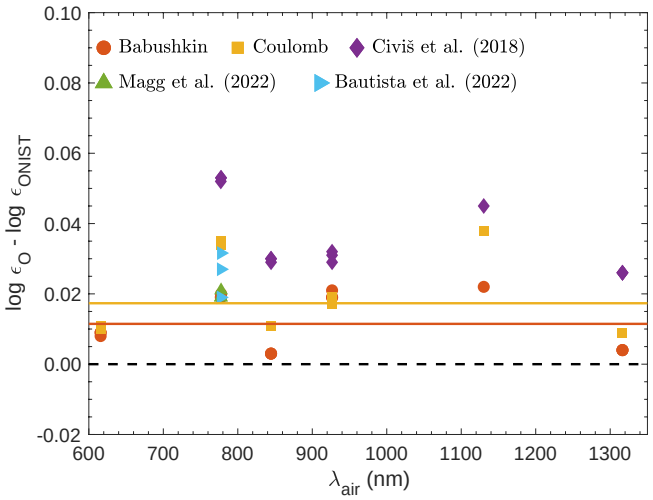

Fig. 5. Solar oxygen abundance differences inferred using different theoretical transition data given in Table 6, relative to the NIST-ASD values. Red circle: Babushkin gauge from present work. Orange square: Coulomb gauge from present work. Purple diamond: Civiš et al. (2018). Green upwards triangle: Magg et al. (2022). Blue right triangle: Bautista et al. (2022). Red and blue solid horizontal lines: Mean result for the Babushkin gauge and Coulomb gauge, respectively. Note: we give equal weights to all *LS* features.

0.01 to 0.03 dex. In both cases, the differences are the largest for the O I 777 nm triplet.

Figure 5 illustrates the results in Table 6 in terms of differences to the solar oxygen abundance via

$$\Delta\log\,\epsilon = -\Delta\,\log\,(gf) = -\left(\log\,(gf)_{\rm new} - \log\,(gf)_{\rm orig}\right), \qquad (5)$$

where, in this case, $\log\,(gf)_{\rm orig}$ corresponds to the $\log\,(gf)$ values from Hibbert et al. (1991) via the NIST-ASD. We see a systematic shift upwards, by 0.011 dex (on average) in the Babushkin gauge and 0.017 dex on average in the Coulomb gauge. In particular, for the O I 777 nm triplet, to which Asplund et al. (2021) gave the largest weight among their selected atomic lines and for which they adopt $\log\,\epsilon_{\rm O} = 8.69$ via the analysis of Amarsi et al. (2018), the inferred abundance increases to $\log\,\epsilon_{\rm O} = 8.71$. This value remains in good agreement with the result those authors obtained from forbidden lines (8.70) and from molecular lines (8.70; see also Amarsi et al. 2021), and it is also within the quoted uncertainty of 0.04.

The result of Amarsi et al. (2018) for the O I 777 nm triplet is 0.06 – 0.08 dex lower than that found by Bergemann et al. (2021, 8.75±0.03) and Magg et al. (2022, 8.77±0.04) from the same spectral feature. As illustrated in Fig. 5, the difference in $\log\,(gf)$ from the multi-method results of Magg et al. (2022) and Bautista et al. (2022), compared to that adopted in Amarsi et al. (2018), amounts to around 0.02−0.03 dex. These differences are significant, but they are not the dominant reason for the 0.06−0.08 dex discrepancies. Further discussion of the origins of these discrepancies may be found in Sect. 4.4 of Amarsi et al. (2021).

Our overall advocated solar oxygen abundance is 8.70 ± 0.04, after taking into account the permitted O I, forbidden [O I], and molecular OH lines, and adopting the same (systematic) uncertainty as given in Asplund et al. (2021). This falls in the 'low' range of values as defined above, and does little to alleviate the solar modelling problem. Rather, the solution to this long-standing problem may in part derive from improvements to the theoretical modelling (Bailey et al. 2015; Buldgen et al. 2017, 2019; Zhang et al. 2019; Yang 2019, 2022).

5. Conclusions

In this work, we computed the extended atomic data including energy levels, lifetimes, and transition data of E1 transitions, in addition to providing them for O I, using MCDHF and RCI methods. These data are indispensable for reliable solar and stellar spectroscopic analyses.

We performed extensive comparisons of the computed transition data with other theoretical and experimental results. The agreement between the computed transition data and the respective results from the NIST-ASD is rather good for most of the transitions, especially for transitions with $A \geq 10^5$ s^{-1} or $\log\,(gf) > -1.5$. 266 out of the 380 selected transitions available in the NIST-ASD are in agreement with the latter within 20%. At the same time, for weaker transitions with $A < 10^5$ or $\log\,(gf) < -1.5$, the discrepencies between different theoretical methods display a much wider scatter. In particular, for transitions with $10^3 \leq A \leq 10^5$ s^{-1} or -3.5 $\leq \log\,(gf) \leq$ -2, the transition data in the Coulomb gauge are in better agreement with the other theoretical values than those in the Babushkin gauge; most of them are transitions involving high Rydberg states, for which we recommend the radiative data in the Coulomb gauge from this work. The computed lifetimes and oscillator strengths, $\log\,(gf)$, have also been compared with available results from experimental measurements. Our computed values (in either gauge) are in good overall agreement with the measured values.

In addition, we used four methods to estimate the uncertainties of the computed transition probabilities, based on the relative differences of the computed transition rates in the Babushkin and Coulomb gauges, given by the quantity of dT and by CF. Based on the accuracy classes predicted from max(dT, d$T_{\rm av}$), 205 out of 989 computed transitions are with uncertainty less than 10% and assigned to the accuracy classes A or B. All of the computed transitions belonging to the AA accuracy class are rather strong with $A \geq 10^6$ s^{-1}. All the transitions with $A \geq 10^6$ s^{-1} are associated with uncertainties less than 25%; while for weak transitions with $A < 10^2$ s^{-1}, most are assigned to accuracy classes D or E.

Finally, the impact of the new atomic data on oxygen abundance analyses was analysed by applying corrections $\Delta\log\,\epsilon = -\Delta\,\log\,(gf)$ to literature abundances.. In general, the transition probabilities for typical O I lines are underestimated by Civiš et al. (2018), but overestimated by Hibbert et al. (1991). For the O I 777 nm triplet, the differences with respect to our results in the Babushkin gauge are −0.03 dex and +0.02 dex, respectively. Our transition probabilities combined with the analysis of the O I 777 nm triplet presented by Amarsi et al. (2018) suggest $\log\,\epsilon_{\rm o} = 8.71$ for the Sun. This is in excellent agreement with low-excitation forbidden lines, as well as molecular lines. Overall, we advocate for the value of $\log\,\epsilon_{\rm o} = 8.70 \pm 0.04$.

Acknowledgements. A.M.A. gratefully acknowledges support from the Swedish Research Council (VR 2020-03940). M.C.L. would like to acknowledge the support from the Guangdong Basic and Applied Basic Research Foundation (2022A1515110043). We would like to thank the anonymous referee for his/her useful comments that helped to improve the original manuscript.

References

Allende Prieto, C., Lambert, D. L., & Asplund, M. 2001, ApJ, 556, L63
Amarsi, A. M., Asplund, M., Collet, R., & Leenaarts, J. 2016, MNRAS, 455, 3735

Amarsi, A. M., Barklem, P. S., Asplund, M., Collet, R., & Zatsarinny, O. 2018, A&A, 616, A89
Amarsi, A. M., Grevesse, N., Asplund, M., & Collet, R. 2021, A&A, 656, A113
Anders, E., & Grevesse, N. 1989, Geochim. Cosmochim. Acta, 53, 197
Asplund, M., & García Pérez, A. E. 2001, A&A, 372, 601
Asplund, M., Grevesse, N., Sauval, A. J., Allende Prieto, C., & Kiselman, D. 2004, A&A, 417, 751
Asplund, M., Grevesse, N., & Sauval, A. J. 2005, ASP Conf. Ser., 336, 25
Asplund, M., Amarsi, A. M., & Grevesse, N. 2021, A&A, 653, A141
Bacławski, A. 2008, J. Quant. Spec. Radiat. Transf., 109, 1986
Bailey, J. E., Nagayama, T., Loisel, G. P., et al. 2015, Nature, 517, 56
Bautista, M. A., Bergemann, M., Gallego, H. C., et al. 2022, A&A, 665, A18
Bergemann, M., Hoppe, R., Semenova, E., et al. 2021, MNRAS, 508, 2236
Bertran de Lis, S., Delgado Mena, E., Adibekyan, V. Z., Santos, N. C., & Sousa, S. G. 2015, A&A, 576, A89
Biemont, E., & Zeippen, C. J. 1992, A&A, 265, 850
Bischel, W. K., Perry, B. E., & Crosley, D. R. 1981, Chem. Phys. Lett., 82, 85
Bischel, W. K., Perry, B. E., & Crosley, D. R. 1982, Appl. Opt., 21, 1419
Boesgaard, A. M., King, J. R., Deliyannis, C. P., & Vogt, S. S. 1999, AJ, 117, 492
Bridges, J. M., & Wiese, W. L. 1998, Phys. Rev. A, 57, 4960
Bromander, J., Duric, N., Erman, P., & Larsson, M. 1978, Phys. Scr, 17, 119
Brooks, N. H., Rohrlich, D., & Smith, W. H. 1977, ApJ, 214, 328
Buder, S., Sharma, S., Kos, J., et al. 2021, MNRAS, 506, 150
Buldgen, G., Salmon, S. J. A. J., Noels, A., et al. 2017, A&A, 607, A58
Buldgen, G., Salmon, S. J. A. J., Noels, A., et al. 2019, A&A, 621, A33
Butler, K., & Zeippen, C. J. 1991, J. Phys. IV France, 01, C1
Caffau, E., Ludwig, H. G., Steffen, M., et al. 2008, A&A, 488, 1031
Caffau, E., Ludwig, H. G., Steffen, M., et al. 2015, A&A, 579, A88
Christensen-Dalsgaard, J. 2021, Living Rev. Solar Phys., 18, 2
Civiš, S., Kubelík, P., Ferus, M., et al. 2018, ApJS, 239, 11
Clyne, M. A. A., & Piper, L. G. 1976, J. Chem. Soc., Faraday Trans. 2, 72, 2178
Cowan, R. D. 1981, The Theory of Atomic Structure and Spectra (Berkeley, CA: University of California Press)
Cubas Armas, M., Asensio Ramos, A., & Socas-Navarro, H. 2020, A&A, 643, A142
Day, R. L., Anderson, R. J., & Salamo, G. J. 1981, J. Opt. Soc. Am., 71, 851
Delgado Mena, E., Adibekyan, V., Santos, N. C., et al. 2021, A&A, 655, A99
Druetta, M., & Poulizac, M. C. 1970, Phys. Lett. A, 33, 115
Dyall, K., Grant, I., Johnson, C., Parpia, F., & Plummer, E. 1989, Comput. Phys. Commun., 55, 425
Eissner, W. 1991, J. Phys. IV France, 01, C1
Ekman, J., Godefroid, M., & Hartman, H. 2014, Atoms, 2, 215
El-Sayed, F. 2021, J. Quant. Spectrosc. Radiative Transfer, 276, 107930
Franchini, M., Morossi, C., Di Marcantonio, P., et al. 2021, AJ, 161, 9
Froese Fischer, C. 2000, Comput. Phys. Commun., 128, 635
Froese Fischer, C. 2009, Physica Scripta T, 134, 014019
Froese Fischer, C., Tachiev, G., Gaigalas, G., & Godefroid, M. R. 2007, Comput. Phys. Commun., 176, 559
Froese Fischer, C., Godefroid, M., Brage, T., Jönsson, P., & Gaigalas, G. 2016, J. Phys. B: At. Mol. Opt. Phys., 49, 182004
Froese Fischer, C., Gaigalas, G., Jönsson, P., & Bieroń, J. 2019, Comput. Phys. Commun., 237, 184
Gaigalas, G., Rudzikas, Z., & Froese Fischer, C. 1997, J. Phys. B: At. Mol. Phys., 30, 3747
Gaigalas, G., Fritzsche, S., & Grant, I. P. 2001, Comput. Phys. Commun., 139, 263
Gaigalas, G., Rynkun, P., Radžiūtė, L., et al. 2020, ApJS, 248, 13
Gaillard, M., & Hesser, J. E. 1968, ApJ, 152, 695
Goldbach, C., & Nollez, G. 1994, A&A, 284, 307
Golly, A., Jazgara, A., & Wujec, T. 2003, Phys. Scr, 67, 485
Grant, I. P. 1974, J. Phys. B: At. Mol. Phys., 7, 1458
Grant, I. P. 2007, Relativistic Quantum Theory of Atoms and Molecules (New York: Springer)
Hibbert, A. 1974, J. Phys. B: At. Mol. Phys., 7, 1417
Hibbert, A. 1975, Comput. Phys. Commun., 9, 141
Hibbert, A., Biemont, E., Godefroid, M., & Vaeck, N. 1991, J. Phys. B: At. Mol. Opt. Phys., 24, 3943
Israelian, G., García López, R. J., & Rebolo, R. 1998, ApJ, 507, 805
Jenkins, D. B. 1985, J. Quant. Spec. Radiat. Transf., 34, 55
Johnson, C. E. 1972, Phys. Rev. A, 5, 2688
Jönsson, P., Godefroid, M., Gaigalas, G., et al. 2022, Atoms, 11, 7
Jönsson, P., Gaigalas, G., Froese Fischer, C., et al. 2023, Atoms, 11, 68
Kikuchi, T. T. 1971, Appl. Opt., 10, 1288
Kolecki, J. R., & Wang, J. 2022, AJ, 164, 87
Korotin, S. A., Andrievsky, S. M., Luck, R. E., et al. 2014, MNRAS, 444, 3301
Kramida, A. 2014, Atoms, 2, 86
Kramida, A. 2023, NIST atomic transition probability bibliographic database (version 9.0), Online at https://doi.org/10.18434/T46C7N
Kramida, A., Ralchenko, Y., Reader, J., & NIST ASD Team 2022, NIST Atomic Spectra Database (ver. 5.10), Available: https://physics.nist.gov/asd
Kröll, S., Lundberg, H., Persson, A., & Svanberg, S. 1985, Phys. Rev. Lett., 55, 284
Lawrence, G. M. 1970, Phys. Rev. A, 2, 397
Li, W., Amarsi, A. M., Papoulia, A., Ekman, J., & Jönsson, P. 2021, MNRAS, 502, 3780
Li, M. C., Li, W., Jönsson, P., Amarsi, A. M., & Grumer, J. 2023, ApJS, 265, 26
Lin, C. C., Irwin, D. J. G., Kernahan, J. A., Livingston, A. E., & Pinnington, E. H. 1972, Can. J. Phys., 50, 2496
Magg, E., Bergemann, M., Serenelli, A., et al. 2022, A&A, 661, A140
Martinson, I., Berry, H. G., Bickel, W. S., & Oona, H. 1971, J. Opt. Soc. Am., 61, 519
Mason, J. W. 1990, Science, 252, 5008
Meléndez, J., & Asplund, M. 2008, A&A, 490, 817
Meléndez, J., & Barbuy, B. 2002, ApJ, 575, 474
Mondet, G., Blancard, C., Cossé, P., & Faussurier, G. 2015, ApJS, 220, 2
Nissen, P. E., Chen, Y. Q., Carigi, L., Schuster, W. J., & Zhao, G. 2014, A&A, 568, A25
Nowak, G., Borst, W. L., & Fricke, J. 1978, Phys. Rev. A, 17, 1921
Olsen, J., Roos, B. O., Jørgensen, P., & Jensen, H. J. A. 1988, J. Chem. Phys., 89, 2185
Ott, W. R. 1971, Phys. Rev. A, 4, 245
Papoulia, A., Ekman, J., Gaigalas, G., et al. 2019, Atoms, 7, 106
Pinnington, E. H., Irwin, D. J. G., Livingston, A. E., & Kernahan, J. A. 1974, Can. J. Phys., 52, 1961
Romano, D. 2022, A&ARv, 30, 7
Savage, B. D., & Lawrence, G. M. 1966, ApJ, 146, 940
Smith, W. H., Bromander, J., Curtis, L. J., Berry, H. G., & Buchta, R. 1971, ApJ, 165, 217
Socas-Navarro, H. 2015, A&A, 577, A25
Steffen, M., Prakapavičius, D., Caffau, E., et al. 2015, A&A, 583, A57
Sturesson, L., Jönsson, P., & Froese Fischer, C. 2007, Comput. Phys. Commun., 177, 539
Tachiev, G. I., & Froese Fischer, C. 2002, A&A, 385, 716
Tayal, S. S. 2009, Physica Scripta, 79, 015303
Vinyoles, N., Serenelli, A. M., Villante, F. L., et al. 2017, ApJ, 835, 202
Wells, W. C., & Zipf, E. C. 1974, Phys. Rev. A, 9, 568
Wiese, W. L., Fuhr, J. R., & Deters, T. M. 1996, Journal of Physical and Chemical Reference Data, Monograph 7 (Melville, NY: AIP Press)
Yang, W.-M. 2019, ApJ, 873, 18
Yang, W.-M. 2022, ApJ, 939, 61
Zhang, Q.-S., Li, Y., & Christensen-Dalsgaard, J. 2019, ApJ, 881, 103
Zhang, X.-Y., Shen, X.-Z., Yuan, P., & Hu, F. 2020, Phys. Rev. A, 102, 042824
Zheng, N.-W., & Wang, T. 2002, ApJS, 143, 231

Appendix A: Energy levels and transition data for O I.

Table A.1. Energy levels (in cm^{-1}), lifetimes (in s; given in Babushkin (τ_B), and Coulomb (τ_C) gauges) for O I.

No.	State	$E_{\rm MCDHF}$	$E_{\rm NIST}$	ΔE	τ_B	τ_C
1	$2s^2 2p^4\ ^3P_2$	0.00	0.000	0		
2	$2s^2 2p^4\ ^3P_1$	155.73	158.265	2.54		
3	$2s^2 2p^4\ ^3P_0$	223.26	226.977	3.72		
4	$2s^2 2p^4\ ^1D_2$	15966.11	15867.862	-98.25		
5	$2s^2 2p^4\ ^1S_0$	34053.62	33792.583	-261.04		
6	$2s^2 2p^3 3s\ ^5S^o_2$	73705.01	73768.200	63.19	2.0918E-04	2.1296E-04
7	$2s^2 2p^3 3s\ ^3S^o_1$	76728.03	76794.978	66.95	1.7020E-09	1.6911E-09
8	$2s^2 2p^3 3p\ ^5P_1$	86455.25	86625.757	170.51	2.9107E-08	3.0123E-08
9	$2s^2 2p^3 3p\ ^5P_2$	86457.22	86627.778	170.56	2.9094E-08	3.0109E-08
10	$2s^2 2p^3 3p\ ^5P_3$	86460.80	86631.454	170.65	2.9070E-08	3.0085E-08
–	–	–	–	–	–	–

Notes. Energy levels are given relative to the ground state and compared with NIST-ASD data (Kramida et al. 2022). Differences, ΔE, between the $E_{\rm MCDHF}$ and $E_{\rm NIST}$ values are shown in the fifth column. Full table is available at the CDS.

Table A.2. Electric dipole transition data for O I.

Upper	Lower	λ (nm)	S (a.u. of $a_0^2e^2$)		log gf		A (s^{-1})		dT	CF		
			B	C	B	C	B	C		B	C	Acc.
$2s^2 2p^3 5d\ ^3D^o_1$	$2s^2 2p^4\ ^3P_2$	94.8686	1.01E-03	9.82E-04	-3.489	-3.502	8.01E+05	7.77E+05	0.030	1.90E-03	3.71E-02	B
$2s^2 2p^3 5d\ ^3D^o_2$	$2s^2 2p^4\ ^3P_2$	94.8686	1.52E-02	1.47E-02	-2.313	-2.327	7.20E+06	6.98E+06	0.030	3.84E-03	1.40E-01	B
$2s^2 2p^3 5d\ ^3D^o_3$	$2s^2 2p^4\ ^3P_2$	94.8686	8.48E-02	8.23E-02	-1.566	-1.579	2.87E+07	2.79E+07	0.030	8.04E-03	3.74E-01	A
$2s^2 2p^3 5d\ ^5D^o_3$	$2s^2 2p^4\ ^3P_2$	94.8898	1.37E-06	1.38E-06	-6.356	-6.354	4.66E+02	4.68E+02	0.006	1.32E-07	6.21E-06	C
$2s^2 2p^3 5d\ ^5D^o_2$	$2s^2 2p^4\ ^3P_2$	94.8898	1.68E-08	1.85E-08	-8.269	-8.226	7.97E+00	8.79E+00	0.094	3.63E-09	1.63E-07	D
$2s^2 2p^3 5d\ ^5D^o_1$	$2s^2 2p^4\ ^3P_2$	94.8898	3.31E-08	3.16E-08	-7.975	-7.994	2.61E+01	2.50E+01	0.044	2.64E-08	8.23E-07	C
$2s^2 2p^3 5d\ ^3D^o_1$	$2s^2 2p^4\ ^3P_1$	95.0112	1.51E-02	1.47E-02	-2.315	-2.328	1.19E+07	1.16E+07	0.030	6.02E-03	2.46E-01	B
$2s^2 2p^3 5d\ ^3D^o_2$	$2s^2 2p^4\ ^3P_1$	95.0112	4.54E-02	4.40E-02	-1.838	-1.851	2.14E+07	2.08E+07	0.030	7.97E-03	3.78E-01	B
$2s^2 2p^3 5d\ ^5D^o_2$	$2s^2 2p^4\ ^3P_1$	95.0325	8.17E-07	8.20E-07	-6.583	-6.581	3.86E+02	3.87E+02	0.003	1.68E-07	7.74E-06	C
$2s^2 2p^3 5d\ ^5D^o_1$	$2s^2 2p^4\ ^3P_1$	95.0325	8.94E-09	9.69E-09	-8.544	-8.509	7.03E+00	7.63E+00	0.078	4.54E-09	2.03E-07	D
–	–	–	–	–	–	–	–	–	–	–	–	

Notes. Upper and lower states, wavelength in vacuum, λ, line strength, S, weighted oscillator strength, log gf, transition probability, A, together with the relative difference between two gauges of A values, dT, and cancellation factor, CF, are shown in the table. Note that the wavelengths and transition parameters are adjusted to the NIST-ASD Ritz wavelength values (Kramida et al. 2022). The limits of the accuracy classes, Acc., are defined as: A ≤ 3%, B ≤ 10%, C ≤ 25%, D ≤ 50%, and E > 50%. Only the first ten rows are shown. Full table is available at the CDS.